Influence of storm surges and sea level on shallow tidal basin erosive processes

G. Mariotti,[1] S. Fagherazzi,[1] P. L. Wiberg,[2] K. J. McGlathery,[2] L. Carniello,[3] and A. Defina[3]

[1]   The finite-element model WWTM is applied to a system of lagoons at the Virginia Coast Reserve, USA. The model solves the shallow water equations to compute tidal fluxes, and is equipped with a wave propagation module to calculate wave height during local wind events. The model is validated using measured water elevations, wave heights, and periods at five locations within the lagoon system. Scenarios with different wind conditions, storm surges, and relative sea level are simulated. Results are analyzed in terms of bottom shear stresses on the tidal flats, a measure of sediment resuspension potential, and total wave energy impacting the marsh boundaries, which is the chief process driving lateral marsh erosion. Results indicate that wave energy at the marsh boundaries is more sensitive to wind direction than are bottom shear stresses. Wave energy on marsh boundaries and bottom shear stresses on the tidal flats increase with sea level elevation, with the former increasing almost ten times more than the latter. Both positive and negative feedbacks between wave energy at the boundaries and bottom shear stresses are predicted, depending on the fate of the sediments eroded from the salt marsh boundaries.

Citation: Mariotti, G., S. Fagherazzi, P. L. Wiberg, K. J. McGlathery, L. Carniello, and A. Defina (2010), Influence of storm surges and sea level on shallow tidal basin erosive processes, *J. Geophys. Res.*, *115*, C11012, doi:10.1029/2009JC005892.

1.   Introduction

[2]   Wind waves are critical for the morphological and ecological equilibrium of shallow tidal basins. Two distinct erosional mechanisms are associated with wind waves. Wave-generated shear stresses, combined with tidal currents, are the main mechanism responsible for sediment resuspension on tidal flats [*Carniello et al.*, 2005; *Fagherazzi et al.*, 2006, 2007; *Marani et al.*, 2007], and regulate both sediment concentration in the water column (and hence light availability at the bed) [e.g., *Lawson et al.*, 2007] and sediment export to salt marshes and to the ocean [*Mariotti and Fagherazzi*, 2010]. Waves impacting salt marsh boundaries produce intermittent forces that promote marsh edge erosion and salt marsh regression. Even though marsh boundary erosion is a complex geotechnical problem that is dependent on a variety of processes (unsaturated filtration, root effects, soil characteristics, and bioturbation), evidence shows that waves are the chief driver [*Schwimmer*, 2001; *Moeller et al.*, 1996; *Möller et al.*, 1999].

[3]   Measurements of waves inside shallow tidal basins are generally rare; therefore a direct statistical analysis of the wave climate is seldom possible. A more profitable approach is to model wave fields as a function of forcing parameters, such as tidal elevation and wind characteristics, that are more readily available. In addition, by using a model-based approach we can estimate the wave regime response to changes in forcing factors, such as sea level oscillations or variations in storminess [e.g., *Fagherazzi and Wiberg*, 2009].

[4]   Wave generation depends on the transfer of energy from the wind to the water surface, which is a function of wind characteristics (duration, direction, and speed), water depth, and fetch (the unobstructed distance over which the wind can blow). Fetch itself is a function of the water depth, since at low tide large areas of the tidal basin emerge and reduce the extent of open water available for wave formation. Water depth is a function of bathymetry and water level, the latter of which is primarily a function of tidal forcing and storm surge. It is thus clear that waves, tides, and basin morphology are tightly interconnected.

[5]   *Fagherazzi and Wiberg* [2009] used a simplified model to relate wave conditions to fetch and water depth in shallow tidal basins, in which water level was imposed throughout the whole basin, allowing water depth at each point of the basin to be determined as a function of bathymetry only. The fetch was then calculated for each fixed direction and a semiempirical relationship [*Young and Verhagen*, 1996; *U.S. Army Coastal Engineering Research Center*, 1984] was used to compute wave height for each wind direction and speed. This simplified model allows a characterization of the wave conditions over the entire basin without the need for a hydrodynamic model, but it is subject

[1]Department of Earth Sciences and Center for Computational Science, Boston University, Boston, Massachusetts, USA.
[2]Department of Environmental Sciences, University of Virginia, Charlottesville, Virginia, USA.
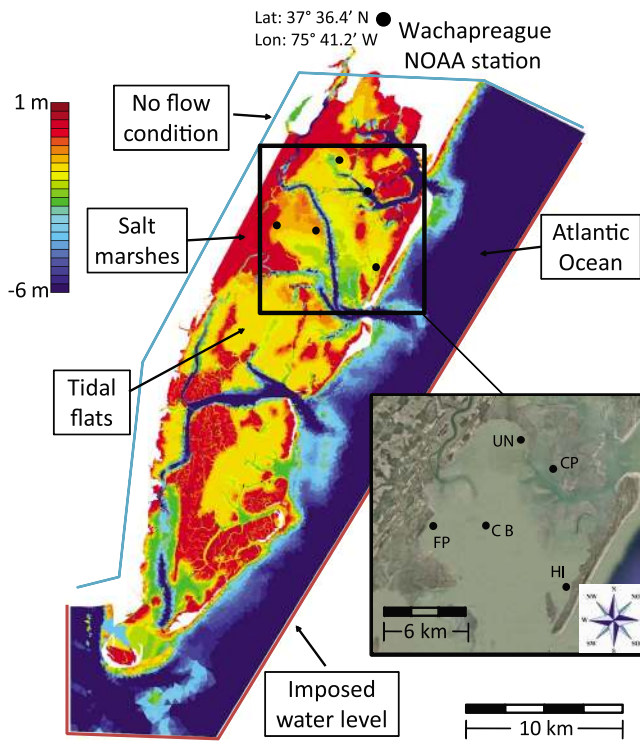[3]Department IMAGE, University of Padova, Padova, Italy.

Figure 1. Bathymetry of the VCR-LTER lagoons. Color indicates ground elevation. Inset shows our measurement sites within Hog Island Bay: FP, Fowling Point; UN, Upshur Neck; CP, Chimney Pole; HI, Hog Island; CB, Center Bay. Position and coordinates of the Wachapreague NOAA station.

to some limitations, including assumptions of (1) uniform water level throughout the basin; (2) steady wave conditions; (3) constant water depth along the fetch during wave propagation; and (4) no interaction between waves and currents.

[6] A full hydrodynamic model is needed to unravel the complex interactions between tidal basin morphology, tides, waves and storms. The two-dimensional finite element model WWTM (Wind Wave Tidal Model) is used herein. The model solves the shallow water equations together with the formation and propagation of local wind waves based on the wave action conservation equation [see *Defina*, 2000; *Carniello et al.*, 2005, 2009a; *D'Alpaos and Defina*, 2007]. The model is applied to a system of shallow lagoons and salt marshes in Virginia, USA, and it is validated with measurements of water levels and waves collected at five different locations within the lagoons. The model is then run with different hydrodynamic forcings (winds and tides) to calculate synthetic parameters that describe the erosion of the tidal flats and marsh boundaries. Finally, the model is used to infer the effects of relative sea level rise (RSLR) on these erosional parameters, as well as to predict the morphological evolution of the entire tidal basin.

2. Site Description

[7] The study site is a system of shallow lagoons within the Virginia Coast Reserve (VCR), located on the Atlantic side of the Delmarva Peninsula, USA. The VCR hosts a Long Term

Ecological Research (LTER) facility (www.vcrlter.virginia. edu/). The VCR includes a number of shallow lagoons, characterized by shallow tidal flats (about 1 m below MLLW) and deep channels (about 10 m below MSL), and is bordered by emergent salt marshes (above MSL). The lagoons comprise intertidal and subtidal basins located between the barrier islands and the Delmarva Peninsula. Each basin is connected to the Atlantic Ocean through tidal inlets. The VCR is typical of shallow coastal barrier-lagoon-marsh systems that dominate the Atlantic and Gulf coasts of the USA. According to the hypsographic analysis of *Oertel* [2001], the lagoon is covered by salt marshes (30%), tidal flats (61%), and channels (9%).

[8] Tides are semidiurnal, with a mean tidal range of 1.2 m. Mean higher high water (MHHW) at Wachpreague channel (NOAA station 8631044, Figure 1) is 0.68 m above mean sea level, whereas mean lower low water (MLLW) is −0.70 m. During storm surges both high water and low water are modified, depending on wind intensity and direction, and on atmospheric pressure variations. The highest water level on record is 2.02 m above MSL (5 February 1998) whereas the lowest is −1.56 m above MSL (16 March 1980) (Wachapreague NOAA station, from 28 June 1978 to present). The current rate of relative sea level rise in the region is 3.8–4.0 mm yr^{-1} [*Nerem et al.*, 1998; *Oertel et al.*, 1989; *Emory and Aubrey*, 1991], and is among the highest rates recorded along the Atlantic Coast.

[9] Storms are the primary agent of short-term disturbance in this coastal region. On average, over 20 extratropical storms rework the landscape each year [*Hayden et al.*, 1995]. Marsh vegetation on the salt marshes is dominated by *Spartina alterniflora*, with an average stem height of 30 cm and a height range between 50 and 100 cm. The shallow depths of the VCR make lagoon-bottom sediment ($D_{50} \approx 63$ μm with sorting coefficient $(D_{84}/D_{50})^{1/2} \approx 2$) susceptible to wind-driven waves and currents, thus promoting sediment resuspension [*Lawson et al.*, 2007; *Lawson*, 2004] tides alone are generally insufficient to resuspend sediment from the lagoon bottom.

3. Model Description

[10] The hydrodynamic model WWTM solves the shallow water equations modified through the introduction of a refined subgrid model of topography to deal with flooding and drying processes in irregular domains [*Defina*, 2000; *D'Alpaos and Defina*, 2007]. The numerical model, which uses a finite-element technique and discretizes the domain with triangular elements, has been tested extensively in recent years in the Venice lagoon, Italy [*Carniello et al.*, 2005, 2009a; *D'Alpaos and Defina*, 2007; *Defina et al.*, 2007].

[11] The governing equations for the hydrodynamic model are:

$$\frac{\partial q_x}{\partial t} + \frac{\partial}{\partial x}\left(\frac{q_x^2}{Y}\right) + \frac{\partial}{\partial y}\left(\frac{q_y q_x}{Y}\right) - \left(\frac{\partial R_{xx}}{\partial x} + \frac{\partial R_{xy}}{\partial y}\right) + \frac{\tau_{bx}}{\rho} - \frac{\tau_{wx}}{\rho} + gY\frac{\partial h}{\partial x} = 0$$

$$\frac{\partial q_y}{\partial t} + \frac{\partial}{\partial x}\left(\frac{q_x q_y}{Y}\right) + \frac{\partial}{\partial y}\left(\frac{q_y^2}{Y}\right) - \left(\frac{\partial R_{xy}}{\partial x} + \frac{\partial R_{yy}}{\partial y}\right) + \frac{\tau_{by}}{\rho} - \frac{\tau_{wy}}{\rho} + gY\frac{\partial h}{\partial y} = 0$$

$$\eta\frac{\partial h}{\partial t} + \frac{\partial q_x}{\partial x} + \frac{\partial q_y}{\partial y} = 0$$

$$(1)$$

where t denotes time, q_x and q_y are the flow rates per unit width in the x and y horizontal directions, R_{ij} are the Reynolds stresses (i, j denoting either the x or y coordinates), $\boldsymbol{\tau_b} = (\tau_{bx}, \tau_{by})$ is the bottom stress produced by tidal currents, $\boldsymbol{\tau_w} = (\tau_{wx}, \tau_{wy})$ is the wind shear stress at the water surface, ρ is fluid density, h is the free surface elevation, g is the gravity. Y is the equivalent water depth, defined as the volume of water per unit area actually ponding the bottom, η is the local fraction of wetted domain, accounting for the actual area that can be wetted or dried during a tidal cycle. More details on the wetting and drying scheme are given by *Defina* [2000]. In equation (1), the bottom shear stress $\boldsymbol{\tau_b}$ is computed as

$$(\tau_{bx}, \tau_{by}) = \frac{\sqrt{q_x^2 + q_y^2}}{K_S^2 Y^{4/3}}(q_x, q_y) \qquad (2)$$

where K_S is the Strickler bed roughness coefficient.

[12] For the wind-wave model, the wave action conservation equation is solved following a parameterized approach [*Holthuijsen et al.*, 1989] and using a finite volume scheme. The wind-wave model is fully coupled with the hydrodynamic module [see *Carniello et al.*, 2005, 2009a]. Assuming the direction of wave propagation adjusts instantaneously to the wind direction, the parameterized wave action conservation equation reads:

$$\frac{\partial N}{\partial t} + \frac{\partial}{\partial x} c_{gx} N + \frac{\partial}{\partial y} c_{gy} N = S \qquad (3)$$

where N is the zero-order moment of the wave action spectrum, defined as the ratio between wave energy E and the relative wave frequency σ, averaged over frequency, and c_{gx} and c_{gy} are the group celerity components. S is the source term which takes into account all the physical processes contributing to wave energy, and it is described by the following equation:

$$S = S_w - S_{bf} - S_{wc} - S_{brk} \qquad (4)$$

where S_w is the wave growth by wind action on the water surface, and the other terms describe the dissipation of wave energy by bottom friction (S_{bf}), white-capping (S_{wc}) and depth-induced breaking (S_{brk}). The source term can be expressed as a function of wind speed, water depth, and wave energy as:

$$S = \alpha + \beta N - 2C_f \frac{k}{\sinh(2kY)} N - c\sigma \left(\frac{\gamma}{\gamma_{PM}}\right)^m N$$
$$- \frac{2a}{T_p} Q_b \left(\frac{H_{\max}}{H}\right)^2 N \qquad (5)$$

The values of the parameters α and β depend on the wind speed U; C_f is a friction coefficient, γ is the integral wave steepness parameter, i.e., $\gamma = E\sigma^4/g^2$, γ_{PM} is the theoretical value of γ for a Pearson-Moskowitz spectrum, Q_b is the probability that waves with height H will break, T_p is the wave period, c, m and α are empirical parameters. The numerical values of the parameters used to solve equation (5) are reported by *Carniello et al.* [2005] and *Fagherazzi et al.* [2006].

[13] Following the approach suggested by *Carniello et al.* [2009a], the space and time variation of the peak wave period T_p (which was assumed to be constant by *Carniello et al.* [2005]) is related to the local and instantaneous water depth and wind speed. The peak wave period is then computed, at each time step and at each grid point with the following empirical equation relating the wave period to the local water depth and wind speed [*Young and Verhagen*, 1996; *Breugem and Holthuijsen*, 2007]

$$\tilde{T} = 5\tilde{Y}^{0.375} \qquad (6)$$

where $\tilde{T} = gT_p/U_{wind}$ and $\tilde{Y} = gY/U_{wind}^2$ are the dimensionless wave period and water depth and U_{wind} is wind speed (measured at an elevation of 10 m above still water level).

[14] The model mesh consists of 68,000 triangular elements and 35,000 nodes, and covers an area of approximately 60 km × 20 km (Figure 1). The area inside the bay is approximately 500 km^2. Element size ranges on average from 100 to 200 m, with the smallest elements close to 10 m. As a boundary condition, we impose the water elevation at the seaward boundary of the model domain; zero flux conditions are imposed at the landward boundary. Wind characteristics (speed and direction) are imposed uniformly throughout the whole basin. Three different values for the Strickler roughness coefficient are used in equation (2): 15 m$^{1/3}$/s for the salt marsh, 20 m$^{1/3}$/s for the tidal flats, 25 m$^{1/3}$/s for the channels and the shelf outside the barrier islands. The drag coefficient C_d is related to the Strickler coefficient K_S by $C_d = gY^{-1/3} K_S^{-2}$, resulting in the following values of C_d for the given K_s (fixing the water depth Y equal to 1 m): 0.043, 0.024, and 0.016. Similar values have been used for the Venice lagoon [*Defina*, 2000; *Umgiesser et al.*, 2004; *D'Alpaos and Defina*, 2007] a similar tidal environment located in the north-east of Italy. Neither river discharge nor atmospheric precipitation are taken into account in our simulations.

4. Model Testing

[15] To test the model, we compare its results to field measurements. Two periods are considered for the model testing: Period 1 from 31 January to 5 February 2009 (a total of 144 consecutive hours), and Period 2 from 1 to 2 March 2009 (a total of 72 consecutive hours). Wave events characterized by different wind speeds and directions were present during these periods, permitting us to evaluate the model response, particularly the wave module performance, under different conditions.

[16] Water level was measured with high resolution piezoresistive transducers (RBR© TGR 2050P and Nortek© Aquadopp profilers). The instruments were deployed at five sites (Figure 1): four of them close to the marsh boundary (Upshur Neck, UN, Chimney Pole, CP, Fowling Point, FP, Hog Island, HI), and one close to the main channel that dissects the basin (Center Bay, CB). We used RBR sensors at UN, FP, and CB and Nortek Aquadopps at HI and CP. During Period 1, all the instruments were recording; during Period 2, only the RBR instruments were recording. Water level is computed as the average over a sampling interval (RBR instruments recorded every 30 min, averaging over
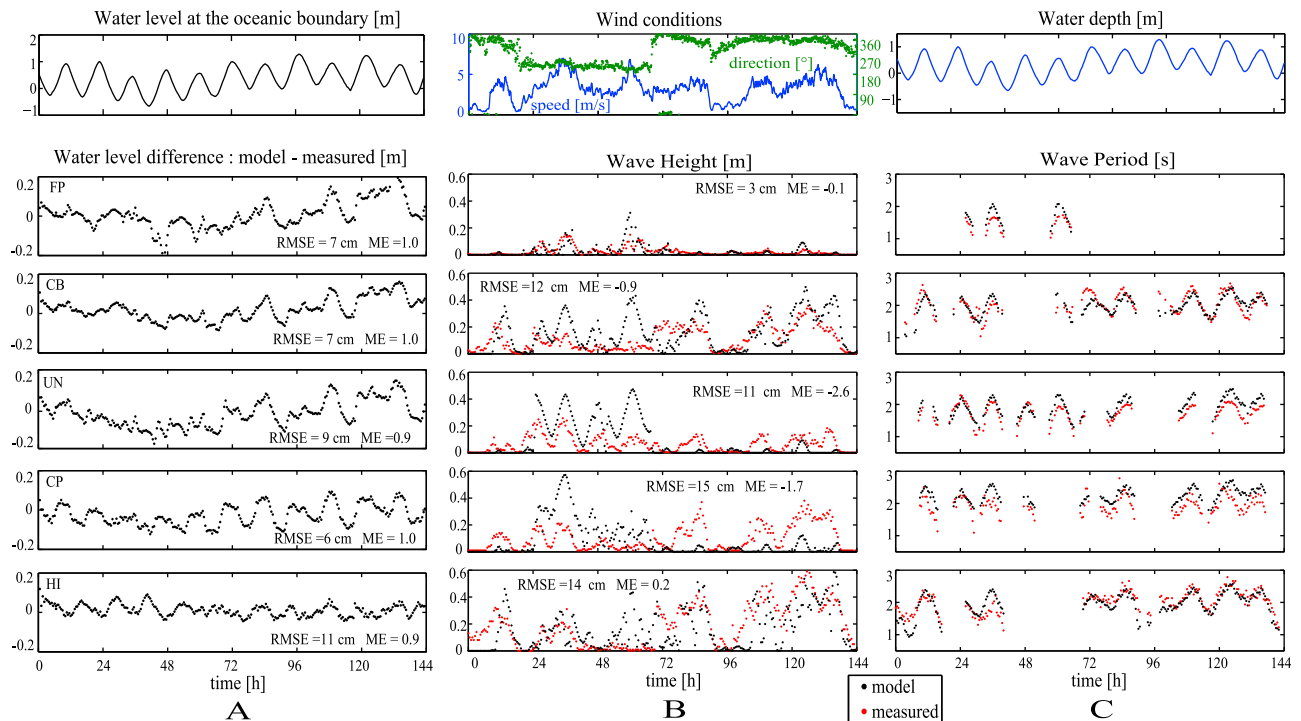
Figure 2. Simulation of Period 1 (from 31 January to 5 February 2009). Water level (referred to MSL) imposed at the seaward boundary (a) water depth, (b) wave height, and (c) period measured and computed at the five study sites. Wave period is reported only for measured wave height greater than 0.1 m. Wind speed from the NOAA Wachapreague station ID 8631044.

300 s; Nortek current profilers record every 10 min, averaging over 60 s). Wave data were recorded every 30 min, sampling 512 bursts with a frequency of 2 Hz. From each wave burst a significant wave height (H_s) and peak period (T_p) are calculated from the power spectral density estimate via Welch's periodogram method [*Press et al.*, 1992].

[17] The model is set up to simulate the same hydrodynamic conditions that were present during the measurement periods. The water level in time is imposed at the seaward boundary (Figure 1). Since no records of tidal oscillations exist in that area, the water level is set equal to the value measured inside the basin shifted by a lag time (location HI, just near the tidal inlet, for Period 1, and location CB for Period 2). The lag time is determined by measuring the delay of the water level propagation from the seaward boundary to the instrument location. The wind input data are taken from the NOAA station at Wachapreague station (ID 8631044), where wind speed and direction are collected every 6 min. The wind field is applied uniformly throughout the domain with the same time resolution as the available data. Analysis of the effect of wind speed and direction measured in different locations within the lagoon of Venice in the application of WWTM suggests that assuming a uniform wind field is acceptable, especially in stormy conditions (i.e., $U_{wind} \geq 10$ m/s). However, in some cases, nonuniformity of wind speed and direction can have some impact especially on the wind wave distribution [*Carniello et al.*, 2009a, 2009b].

[18] Two statistics are used to provide an objective evaluation of model performance: the Model Efficiency (ME)

$$ME = 1 - \frac{\sum (D - M)^2}{\sum (D - \overline{D})^2} \qquad (7)$$

which measures the ratio of the model error to variability in observational data, and the root mean squared error (RMSE)

$$RMSE = \sqrt{\sum \frac{(D - M)^2}{n}} \qquad (8)$$

where D is the observational data, $\overline{D}$ is the mean of the observational data and M is the corresponding model estimate [*Allen et al.*, 2007].

[19] Period 1 is characterized by approximately 11 full tidal cycles with a mean tidal amplitude of 1.3 m (Figure 2a). The maximum water level excursion is 1.9 m and is due to the combined effect of the astronomical tide and storm surge. During Period 1 there are three main wind events (Figure 2b): in the first event the wind blows from north (300°–360°) and has a maximum speed of 6 m/s; in the second event the wind blows from southeast (220°) with a maximum speed of 7 m/s; in the third event the wind blows again from north with maximum speed of 7 m/s.

[20] Water levels computed with the model generally are in agreement with measured values (Figure 2a). Water level

oscillations are similar at each measurement site within the basin, and are similar to the water level imposed at the seaward boundary. The tidal signal does not change significantly in shape as it propagates within the basin (the difference between measurement sites is less than 1 cm, on the order of measure error), and only a phase shift is present. From the model simulation the phase shift between the seaward boundary and the measurement sites are: HI 1 h, CP 0.8 h, CB 1.1 h, UN 1.2 h, and FP 1.4 h. For all the station the RMSE is between 7 and 11 cm, while the ME is close to 1.0. The large value of ME is governed by the forcing at the seaward boundary, which strongly controls the water level. Since the difference between the measured and predicted water level has no correlation with the water level, we conclude that the model reproduces correctly the tide oscillation phase lag among the different stations. Also the range of tidal amplitude is well reproduced: both measured and predicted values do not change significantly (few %) inside the basin. The remaining error in the water level is probably due to some additional overharmonics present in the basin not reproduced by the model.

[21] The agreement between computed and measured wave height varies from site to site (Figure 2b). At the CB site, the wave regime is mainly determined by wind speed, since the fetch is approximately constant in every direction and the water depth is not a strong limiting factor (the minimum water depth is 1 m). Wave height variations are reasonably well represented by the model, with a few wave peaks underestimated in the first half of Period #1. At FP, the wave regime is strongly affected by water depth, since the tidal flats emerge at low water levels. Simulated wave heights at this location are similar to measured values. At the other three sites, HI, UN, and CP, all located close to the marsh boundary, the wave regime is controlled strongly by wind speed and direction, and less by water depth. When the wind blows from the salt marsh, the fetch is almost zero and very small waves form even if the wind speed is high. When the wind blows from the open bay toward the salt marsh, the wave height is determined mainly by wind speed. At HI, where relatively higher waves are present, ME is positive, meaning that the model forecast is a better predictor of wave height than the average value of observed wave height. ME is negative for CB and for three of the four sites near the marsh edge (FP, UN, and CP), suggesting that in this case the average value of observed wave height is a better predictor of wave height than the model forecast. We believe that these poor values for ME can be ascribed partly to an inadequate description of the wind field over the lagoon (wind data are measured at the NOAA station which is not located within the lagoon) (see Figure 1). In fact most of the wave peaks are reproduced by the model, except for the middle part of Period 1 at UN and CP, where the measured wave height is almost zero and computed values are between 10 and 40 cm. Since the wind intensity is not zero during that period, the discrepancy between simulations and measurements is probably due wind nonuniformity over the entire basin. Note that during Period 1 wind speed is moderately low and, as stated above, in these conditions wind uniformity is questionable. Waves computed by the model are compared to measured values only where the wave height is greater than 0.1 m.

[22] Measured wave period falls in the range of 1.5–2.5 s, with variations in phase with water depth. The model follows these variations with good agreement.

[23] Period 2 is characterized by approximately four tidal oscillations (Figure 3). Wind direction was relatively constant (around 0°N) and wind speed varied between 5 and 10 m/s, except for several hours when the wind blew at 15 m/s. The model reproduces correctly the tidal oscillations (ME = 1, not reported in the figure). Wave height is reproduced better than during Period 1: ME is between 0.2 and 0.5 in the sites where waves are present, CB and FP (Figure 3a). This result indicates that the model performs better when wind speed is ≥10 m/s, which is significant for the following simulations. Also in this case the period is well predicted by the model.

5. Model Forecasting

[24] We use the model to study the tidal basin response to a variety of hydrodynamic forcing conditions, namely variations in sea level, tides, and wind fields. Since the use of all possible combinations of tidal oscillations and wind conditions is not feasible, only few combinations are chosen. The next section focuses on the choice of the most significant hydrodynamic inputs for the model. In the model simulations described above, water level was imposed outside the basin at the seaward domain boundary (Figure 2) using the data measured inside the lagoon and shifted appropriately in time. To determine the water level to impose on the seaward boundary for the model forecasts, astronomical tidal components measured at the Wachapreague station are used to create a synthetic tidal signal. Since the goal is to simulate the tide outside the lagoon, tidal harmonics deriving from shallow water effects are neglected. All other 27 components are considered (the six greatest components are reported in Table 1). The synthetic tide generated with this method has a very long periodicity, at least equal to the lunar cycle. For computational reasons, is not feasible to run each simulation for such a long period. Therefore, a window of 72 h is used, and is chosen to avoid both extremely high and extremely low oscillations in order to be representative of the whole signal. In addition, the first 24 h of simulations are discarded form the analysis in order to eliminate the transient effect of the initial conditions. Therefore each simulation gives 48 h, i.e., four full tidal cycles, of usable results.

[25] Winds are variable, seldom maintaining a constant speed and direction for longer than several hours. However, the results of a set of numerical experiments performed to assess the impact of wind transients on the wave field show that the impact is moderate because the adaptation time is relatively short (i.e., shorter than 10–15 min). Therefore, for simplicity, all simulations are run with constant wind speed and direction, using four classes of wind (5, 10, 15, and 20 m/s), and 12 directions. Using a constant wind during the simulations allows us to isolate the basin response to each specific wind condition. The results obtained with these simulations can be easily combined with wind statistics (frequency and duration distribution) to infer the basin response to more realistic meteorological conditions.

[26] Although the tide is the main factor controlling water levels, storm surges contribute significantly to water eleva-

Table 1. Values of the Six Largest Astronomical Tide Components at Wachapreague Station (NOAA)

Component	M2	S2	N2	K1	M4	O1
Speed (deg/h)	28.984	30.000	28.440	15.041	57.968	13.943
Amplitude (m)	0.590	0.102	0.126	0.084	0.025	0.087
Phase (deg)	26.8	63.2	16.9	204.0	221.8	216.7

tion during storms. Storm surge is the temporary and local change in water-surface elevation along a shore due to a storm [*Boon*, 2004]. *Tilburg and Garvine* [2004] showed that up to 65% of storm surge in Atlantic City, NJ, could be explained considering just three processes: inverse barometric effect, wind and wave set up, and Ekman transport. The first is due to a change in the atmospheric pressure, the second is induced by the wind blowing across shore, while the third is produced by the wind blowing along shore for an unconfined shoreline.

[27] We perform a statistical analysis to correlate storm surge to three variables: atmospheric pressure, wind speed, and wind direction. For the analysis we use the storm surge data of the Wachapreague station and the meteorological data of the NOAA Station CHLV2 - Chesapeake Light, VA, taken in the period from 1996 to 1999. First we obtain the pressure corrected storm surge (PCSS) applying an inverse barometric correction (IBC). The IBC assumes that each mBar of pressure higher (lower) than the average atmospheric pressure, 1018 mBar, decreases (increases) the sea level of 1 cm. Then we classify the average PCSS binned by 12 wind directions and four wind speed catego-

ries (Figure 4a). We perform the same classification (wind speed and direction) for the pressure (Figure 4b). The PCSS is clearly correlated to the wind direction: the highest storm surge occurs when the wind blows from 50°N, while extremely low water levels occur with wind from 230°N. Because pressure gradients drive winds, it is not surprising to find the barometric effect correlated with wind conditions. However the barometric effect is correlated mainly on wind speed, and only slightly on wind direction.

[28] For any given wind speed and direction, Figure 4 gives the expected PCSS and atmospheric pressure, which can be combined with the IBC to give the expected total storm surge. This procedure is used for each simulation, in order to associate to each wind event its most probable storm surge. Operatively, the storm surge is added as a constant term to the tidal signal at the seaward boundary.

6. Wave Energy and Bottom Shear Stresses

[29] Wind waves and tidal currents produce bottom shear stresses that resuspend sediments in tidal basins.

[30] Bottom shear stress is a nonlinear combination of shear stress from currents (τ_{curr}) and wave (τ_{wave}), which, according to *Soulsby* [1995, 1997]

$$\tau_m = \tau_{wave} + \tau_{curr}\left[1 + 1.2\left(\frac{\tau_{wave}}{\tau_{wave} + \tau_{curr}}\right)^{3.2}\right] \quad (9)$$

where τ_m is the mean total bottom shear stress. Limiting the analysis to monochromatic waves, under the assumption of
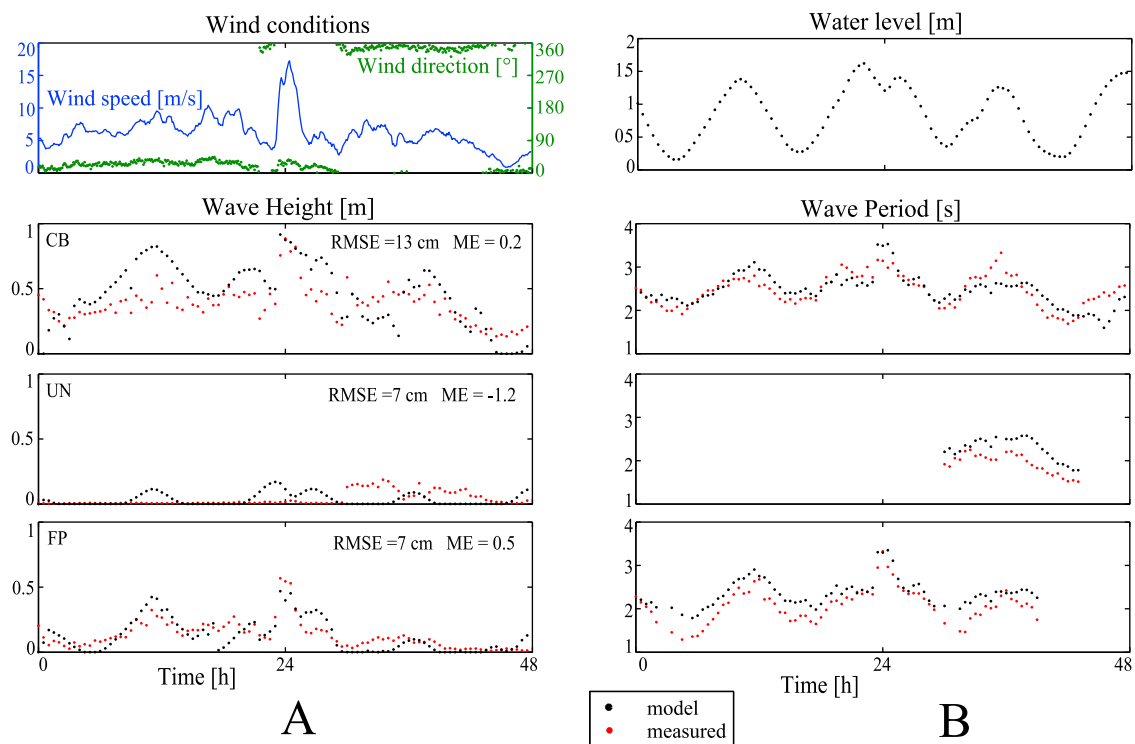

Figure 3. Simulation of Period 2 (from 1 to 2 March 2009). Wind speed from the NOAA Wachapreague station (ID 8631044). Wave height and wave period measured and computed at the five reference sites. Wave period is reported only for measured wave height greater than 0.1 m.
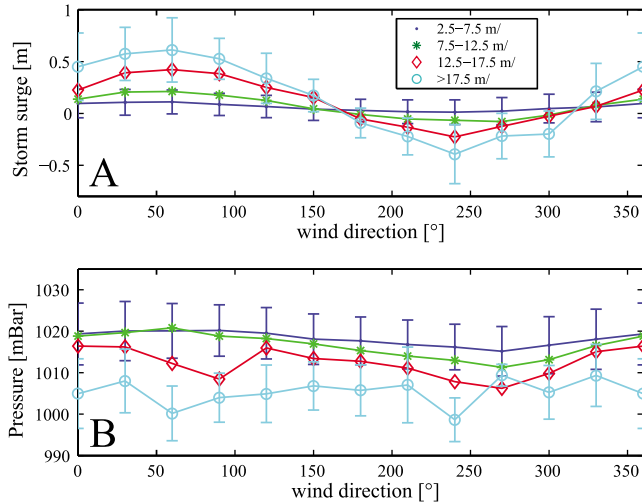
Figure 4. (a) Average pressure corrected storm surge (PCSS). (b) Average atmospheric pressure. Data are binned by 12 wind direction and four wind speed categories. The total storm surge can be calculated by adding the inverse barometric correction (IBC) to the PCSS. For visual clarity error bar are reported only for wind speed of 5 and 20 m/s. Data are from NOAA Station CHLV2, during 1996–1999.

linear wave theory the maximum velocity of wave-induced water motion at the bottom is given by:

$$u_b = \frac{\pi H_s}{T_p \sinh(kY)} \tag{10}$$

and the wave bottom shear stress is given by:

$$\tau_{wave} = \frac{1}{2} f_w \rho u_b^2 \tag{11}$$

with

$$f_w = 0.04 \left[\frac{u_b T_p}{2\pi k_b} \right]^{-0.25} \tag{12}$$

where k is wave number and f_w is a friction factor that depends on the roughness length scale of the sediment bed k_b [*Fredsoe and Deigaard*, 1993]. Herein, we let $k_b = 2D_{90}$ [e.g., *Kamphuis*, 1975], so that equation (9) estimates the skin friction stress, and set $D_{90} = 0.25$ mm based on grain size data from Hog Island Bay [*Lawson*, 2004]. The wave number k can be determined from the dispersion equation derived from linear wave theory:

$$\sigma = \sqrt{gk \tanh(kY)} \tag{13}$$

Bottom shear stress induced by tidal currents is calculated using an equation for uniform flow:

$$\tau_{curr} = C_f \rho U^2 \tag{14}$$

where C_f is a friction coefficient assumed equal to 0.01 [*Fagherazzi et al.*, 2007]. It is worth noting that C_f is not the same at that used in WWTM ($C_d = 0.024$ for tidal flats) where the drag coefficient conceptualize all the processes

responsible for energy dissipation [see *D'Alpaos and Defina*, 2007]. Sediment resuspension is instead related only to the friction induced by currents at the bottom.

[31] The bottom shear stress is calculated only for the tidal flats inside the lagoon, discarding the elements of the mesh representing the creeks, the salt marshes, and the shelf off-shore the barrier islands. For each simulation (four wind speeds × 12 wind directions) bottom shear stresses are calculated at every point of the tidal flat (~20,000 elements) and recorded every 30 min for 48 h. Examples of the wave induced and current induced bottom shear stress distributions, computed for four tide levels (low and high slack water, mid-flood and mid-ebb) are given in Figure 5. The wave induced bottom shear stress is quite uniform across the basin (Figure 5c), and is slightly higher during high water because wave height increases with water depth for a given wind speed (see also Figure 5b). The current induced bottom shear stress is higher at mid-tide, when the water level displacement is fastest, and it is concentrated in the main channels (Figures 5b, 5d). There are no major ebb/flood differences in current induced bottom shear stress either on the tidal flat or in the channels; minor differences are related to the diurnal modulation with greater shear stresses associated to higher tidal excursions (Figure 5b). Shear stresses are higher during ebb than during flood at the southern inlet, while the opposite is true at the northern inlet. This asymmetry is due to a residual circulation with water entering the bay through the northern inlets and leaving through the southern one.

[32] In order to aggregate the data from our simulations, we simultaneously compute the bottom shear stress distribution over time (i.e., over different water levels), for a fixed wind speed of 15 m/s. The same calculation is performed individually for the wave shear stress and the tidal current shear stress (Figure 6). The spatial distribution of wave-induced shear stress is nonmonotonic. The fractional area is almost constant for bottom stresses from 0 to ~0.6 Pa, then increases reaching a peak around 0.8 Pa, and then decreases to zero. No values greater than 1 Pa are present. This distribution reflects the tendency of waves to reach a balance between energy input from the wind and dissipation, so that bottom shear stresses are relatively constant within the tidal flats. The distribution of tidal current shear stress has a negative exponential shape with more than 95% of the basin area under 0.35 Pa. However, the distribution includes locations where the shear stress is higher than the wave induced shear stress, as shown in Figure 5d. This reflects the fact that tidal currents tend to concentrate the flow in selected areas thus increasing shear stresses.

[33] In conclusion, wave induced shear stress is relatively uniform in space and in time (see also Figure 5b), while current induced shear stress is more variable. The distribution of the total shear stress depends on both, as indicated in equation (9); it has the same qualitative behavior as the wave shear stress, but it is broader because of the contribution of the current shear stresses. Wave- and current-induced bottom shear stresses are of the same order of magnitude, approximately 0–1 Pa, and therefore they both affect erosive processes on the tidal flats and need to be included in the analysis.

[34] To better describe the erosion characteristics of the basin, a synthetic parameter is used to aggregate the infor-
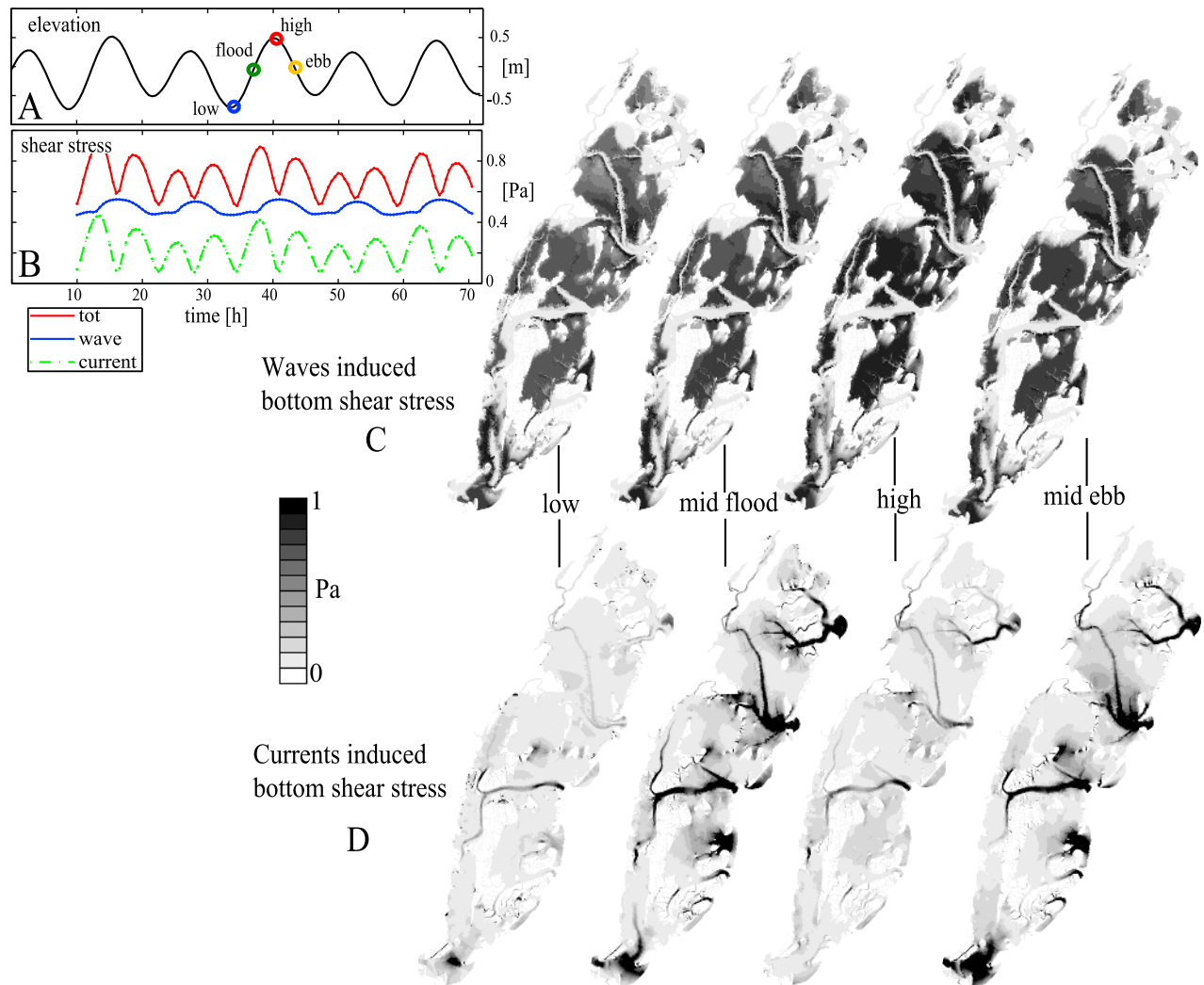
Figure 5. (a) Water level imposed at the seaward boundary. (b–d) Wave-induced and current induced bottom shear stress computed for a wind speed of 15 m/s blowing from 30°N, averaged over the tidal flat area (Figure 5b), and reported at high and low slack water, and mid-ebb and mid-flood tide (Figures 5c and 5d).

mation of the bottom shear stress. An erosion factor EF, similar to the one proposed by *Fagherazzi and Wiberg* [2009], is defined as follows:

$$EF = \frac{\sum_{t=1}^{T}\sum_{i=1}^{N_e} A_i(\tau_m(i,t) - \tau_{cr})}{A_{tf} T} \quad (15)$$

where $\tau_m(i, t)$ is the mean bottom shear stress at time t at a location i which has an area equal to A_i, τ_{cr} is a suitable value of critical shear stress for bottom erosion (values of $\tau_m(i, t) - \tau_{cr} < 0$ are set equal to zero). N_e is the number of mesh elements in the tidal flat, A_{tf} is the area of the tidal flat, and T is the length of the time averaging (48 h). This parameter represents the excess shear stress integrated over the entire basin and averaged over time. The time average is needed to take into account the difference in the bottom shear stress induced by tidal oscillations in water depth. For simplicity, we set τ_{cr} to 0.35 Pa based on measurements and

modeling of sediment erosion and resuspension in the study area [*Lawson*, 2008].

[35] The Erosion Factor is first calculated considering the contribution of current bottom shear stresses (*EFc*) and wave bottom shear stresses (*EFw*) separately. *EFc* has a weak dependence on wind characteristics for wind speeds ≤15 m/s (Figure 7a). Only for higher wind speeds (20 m/s) are the differences in *EFc* significant. In contrast, *EFw* depends strongly on wind speed (Figure 7b): for a wind speed of 5m/s, *EFw* is zero, for wind speeds of 10–15 m/s, values of *EFw* are similar to *EFc*, and for a wind speed of 20 m/s *EFw* is three times *EFc*. *EFw* depends also on wind direction and is greater when the wind blows along the main axis of the basin (N-E to S-W) than when it blows along the minor axis (N-W to S-E). For low wind speed (10–15 m/s) *EFw* shows a central symmetry and is the same for each pair of opposite wind directions. For wind speeds of 20 m/s the symmetry is lost, especially along the major axis, *EFw* is greater for wind blowing from NE than from SW. The range of values assumed by *EFc* and *EFw* and by the current
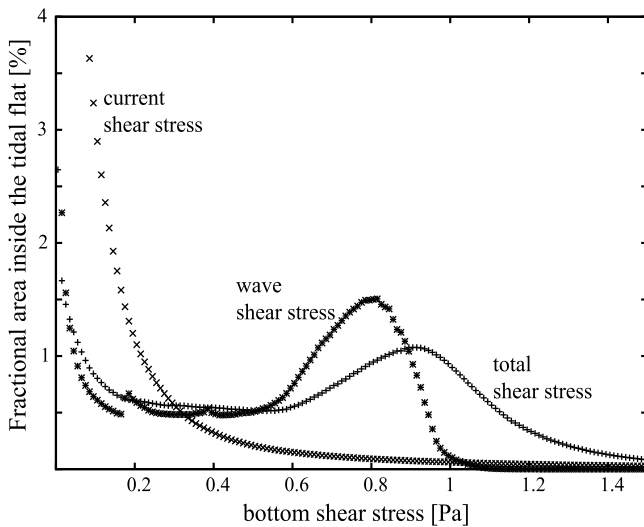
Figure 6. Spatial distribution inside the basin of current-induced, wave-induced and total mean bottom shear stress (equations (8), (10), and (13)), calculated from the results of 12 simulations (wind direction every 30°) with wind speed equal to 15 m/s.

induced and wave induced bottom shear stresses (between 0 and 1 Pa) is comparable to values found in similar studies that employ models [*Le Hir et al.*, 2000; *Cappucci et al.*, 2004; *Fagherazzi et al.*, 2007] and field measurements [*Christie and Dyer*, 1998; *Whitehouse and Mitchener*, 1998].

[36] The total Erosion Factor (*EF*) reflects the contribution of both *EFc* and *EFw*. It strongly depends on wind speed and, in a minor way, on wind direction (Figure 8a). For each wind speed, the difference between the maximum and minimum value of EF is around 20%. EF values are greater when the wind blows along the main axis of the basin (N-E to S-W) than when it blows along the minor axis (N-W to S-E). The ratio between the maximum and minimum EF increases with increasing wind speed.

[37] *Schwimmer* [2001] correlates marsh regression rate to averaged wave power, defined as:

$$P = c_g \frac{\gamma H^2}{8} \tag{16}$$

where γ is the water specific weight and c_g is the wave group celerity given by $c_g = \frac{\sigma}{k} \frac{1}{2}\left(1 + \frac{2kY}{\sinh(2kY)}\right)$, which assumes value in the range 0–2 m/s.

[38] In order to describe the erosion potential by impacting waves at the marsh boundary, we choose the wave power as the main variable. We introduce a Wave Factor at the marsh Boundary, WFB, similar to the erosion factor EF, to synthesize the information given by different hydrodynamic conditions:

$$WFB = \frac{\sum_{t=1}^{T} \sum_{i=1}^{M} L_i(P(i,t) - P_{cr})}{L_{mb}T} \tag{17}$$

where $P(i, t)$ is the wave power at time t at a marsh boundary element i which has a length equal to L_i, M is the number of marsh boundary elements, L_{mb} is the total length

of the marsh boundary, and T is the length of the time averaging (48 h). Similar to bed erosion by shear stresses, we assume that erosion by wave impact is a threshold process, which takes place when the incoming wave power P is greater than a critical value P_{cr}. As for *EF*, the time average is needed to take into account the difference induced by the variable water level through a tidal cycle. This parameter represents the total amount of wave energy per unit of time that reaches the marsh boundary and is dissipated there. Therefore, assuming the erosion rate of the
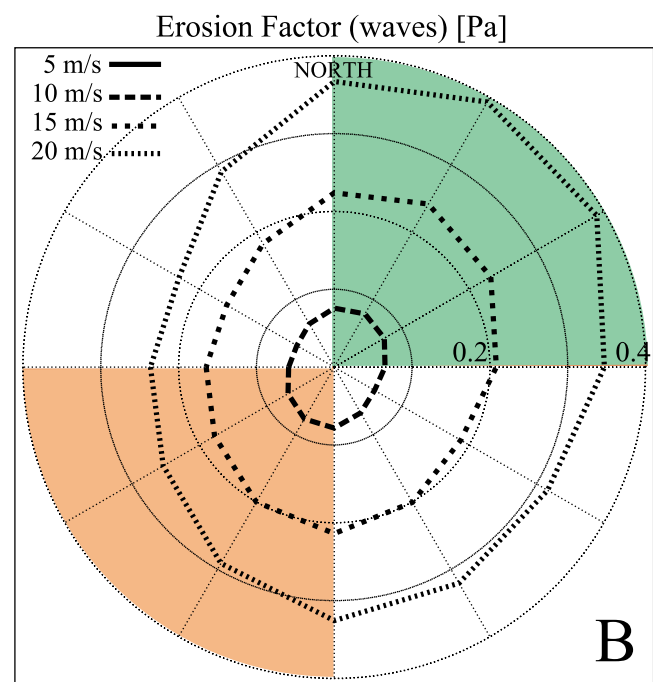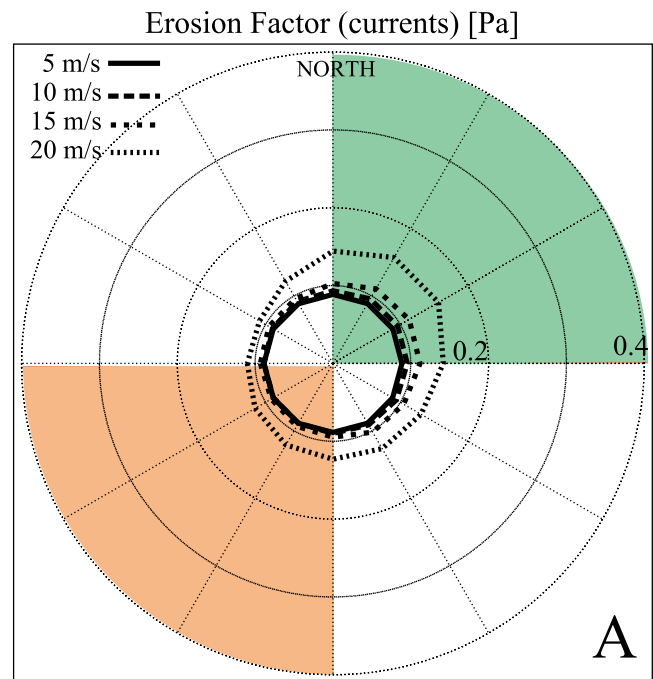

Figure 7. Erosion factor (EF) calculated (a) from current-induced and (b) from wave-induced bottom shear stresses.
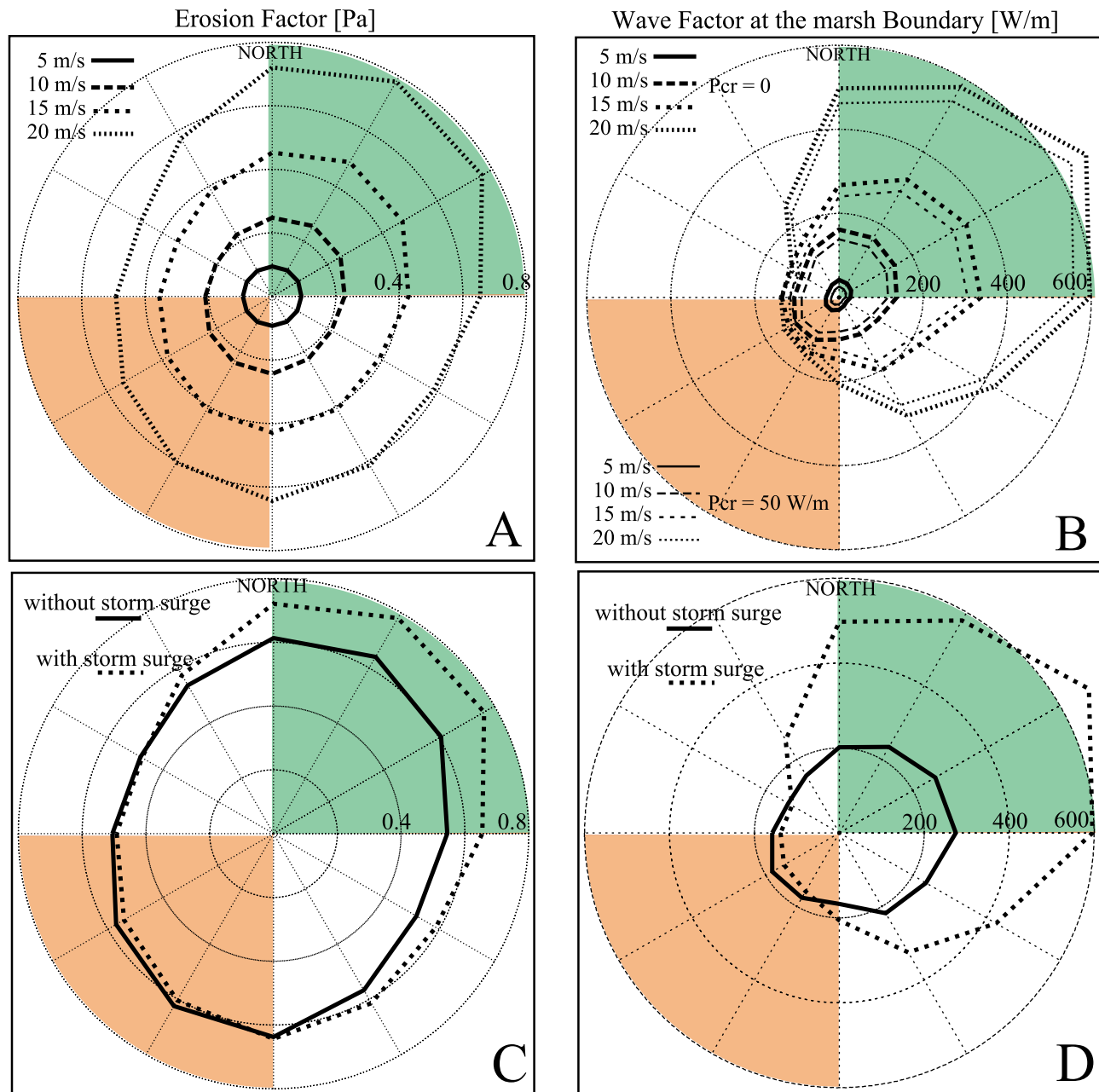
Figure 8. (a) EF and (b) wave factor at the marsh boundary (WFB) calculated for different wind speeds and reported as a function of wind direction. The critical value for bottom shear stress is set equal to 0.35 Pa. WFB is calculated without any threshold values (ticked lines) and with a threshold equal to 50 W/m (thinner lines). Green area represents direction associated predominantly with positive storm surges, red area represents directions associated predominantly with negative storm surges (see Figure 4). (c) EF and (d) WFB calculated for a wind of 20 m/s are compared to simulations that neglect changes in sea level produced by storm surges.

marsh boundary is proportional to this parameter, WFB is a proxy for total marsh boundary retreat within the basin.

[39] We calculate the WFB for several wind speed and directions (Figure 8b), and for two different values of the threshold P_{cr}: 0 and 50 W/m (corresponding approximately to a wave height of 0.2 m). The computed wave power range, from 0 to 600 W/m, is smaller than the range found in a similar work by *Schwimmer* [2001]: 0–10,000 W/m. This difference is probably due to the fact that WFB averages

wave power during the full tidal cycle, taking into account very low water depths, when wave height is strongly reduced. For each fixed wind speed, WFB varies with wind direction. WFB, like EF, is greater when the wind blows along the main axis of the basin (N-E to S-W) than when it blows along the minor axis (N-W to S-E). However, WFB is consistently higher for wind blowing from N-E than for wind blowing from S-W. The difference is more evident when higher wind speeds are considered. Increasing the
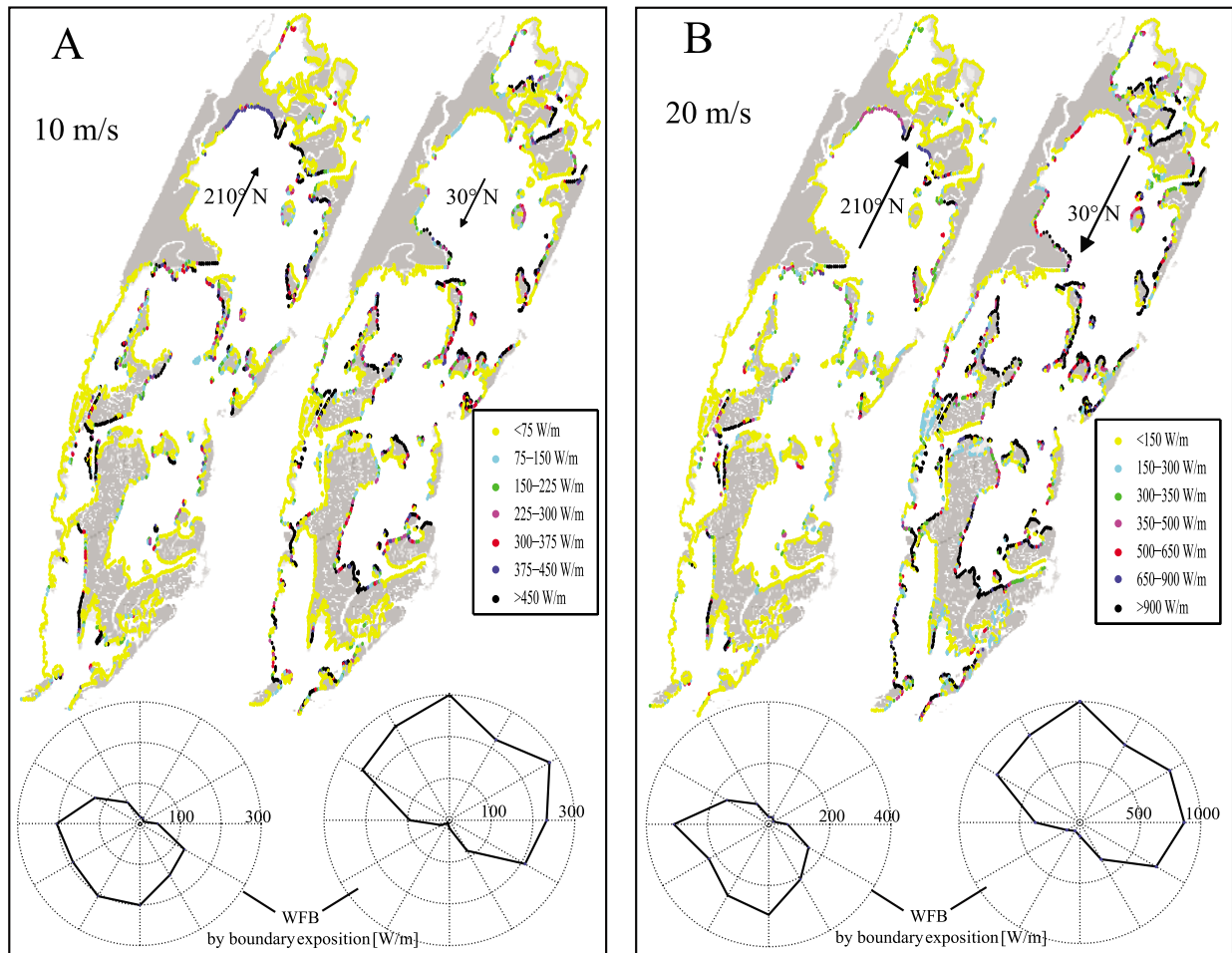
Figure 9. Wave power at the marsh boundary, averaged over 48 h of simulations, calculated for different wind speeds and directions. (a) wind speed of 10 m/s. (b) wind speed 20 m/s. On the bottom WFB, for each wind condition, calculated as a function of marsh exposure.

threshold value P_{cr} decreases values of WFB; however it does not significantly change the WFB dependence on wind regime (speed and direction).

[40] An additional simulation is performed only for a wind speed of 20 m/s, neglecting the superimposition of the storm surge associated with the wind conditions, i.e., using the same water level for each wind direction. Without storm surges the EF is symmetric with respect to the wind direction, resulting in an ellipse with the major axis aligned to the basin main axis (Figure 8c). The presence of a positive storm surge increases the EF up to 30% while a negative storm surge slightly affects it. Even the WFB is more symmetric without storm surges (Figure 8d). The presence of a positive storm surge increases WFB up to 150%, while the presence of a negative storm surge decreases WFB at most by 10%.

[41] The Erosion Factor EF and the Wave Factor at the marsh Boundary WFB permit us to synthesize the effects of waves on sediment mobilization and to understand the relative importance of different wind conditions. This notwithstanding, it is also important to determine the spatial distribution of waves across the tidal flats and at the marsh boundaries in order to define which areas are most prone to erosion. For simplicity we present the spatial distribution of the erosion stresses only for two wind speeds (10 and 20 m/s) and two wind directions (30° and 210° N). To provide an objective evaluation, for each wind condition WFB is calculated as a function of marsh boundary exposure.

[42] The spatial distribution of the wave power at the marsh boundary depends strongly on wind direction (Figure 9). The marsh boundaries facing the wind receive more wave power (quantified in W/m), while the marsh boundaries facing the opposite direction receive almost no wave power. Also the spatial distribution of the wave induced bottom shear stress depends on wind direction (Figure 10a). This dependence is greater close to the marsh boundary where fetch, and consequently wave height, is strongly controlled by wind direction because of the presence of the marshes which prevent wave formation on their leeward sides. The dependence of wave shear stress on wind direction decreases moving away from the marsh boundary, and vanishes after 3–4 km. Wave shear stress is negligible inside the channels because of their large depth compared to the tidal flats. In contrast, the current-induced bottom shear stress is high inside the channels and is negligible on the tidal flat (Figure 10b). The total shear stress, reflecting both contributions, is higher
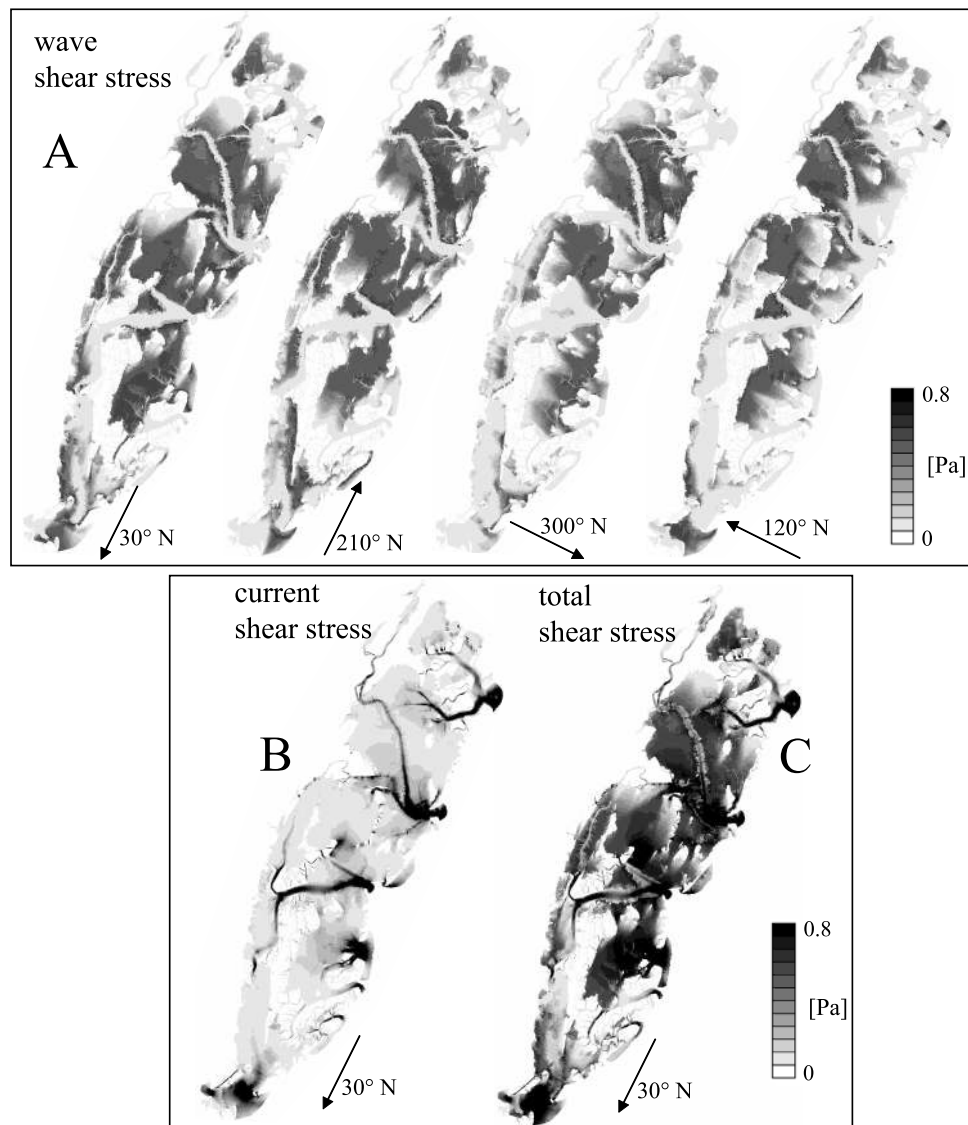
Figure 10. (a) Wave induced bottom shear stress over the tidal flats, averaged over 48 h of simulations, calculated for a wind speed of 10 m/s and four different directions (30, 120, 210, and 300 N). (b) Current induced and (c) total bottom shear stress for a wind speed of 10 m/s blowing from 30°N.

both far from the marsh boundaries and inside the channels (Figure 10c).

7. Wind Statistics and Wave Action

[43] Intertidal areas are subject to varying wind conditions and consequently to a range of erosion events, whose combination leads to their morphological evolution. To provide a reliable estimate of the erosion stresses and wave energy to which the basin is subjected, it is necessary to correctly weight the relative importance of the different wind directions and intensities, according to their probability of occurrence at each coastal location.

[44] We assume that the wind statistics in the years 1996–1999 are representative of the local meteorological conditions (Figure 11a). The distribution of wind direction is not bimodal, with winds from 180°–210°N and 330°–60°N being more frequent.

[45] Values of bottom shear stress and wave power at the marsh boundary are weighted by the relative frequency of occurrence of the different wind conditions. This weighting allows us to calculate the expected (or actual) erosion stresses, i.e., the most probable value of bottom shear stress and wave power in the basin. The expected bottom shear stress is greatest in the channels, especially near the inlets (Figure 11b). Across the tidal flats, the expected bottom shear stress is quite homogeneous. Slightly higher values are found in the middle of the tidal flat, far from the marsh boundary. This happens because the EF is weighted over different wind directions, and therefore the area situated far from the boundary, which has the greatest fetch independently of wind direction, has on average higher waves.

[46] The wave energy at the marsh boundary in contrast displays a clear pattern (Figure 11c), with the highest values found on the marsh boundaries exposed toward the northeast. The asymmetry increases when the threshold value for
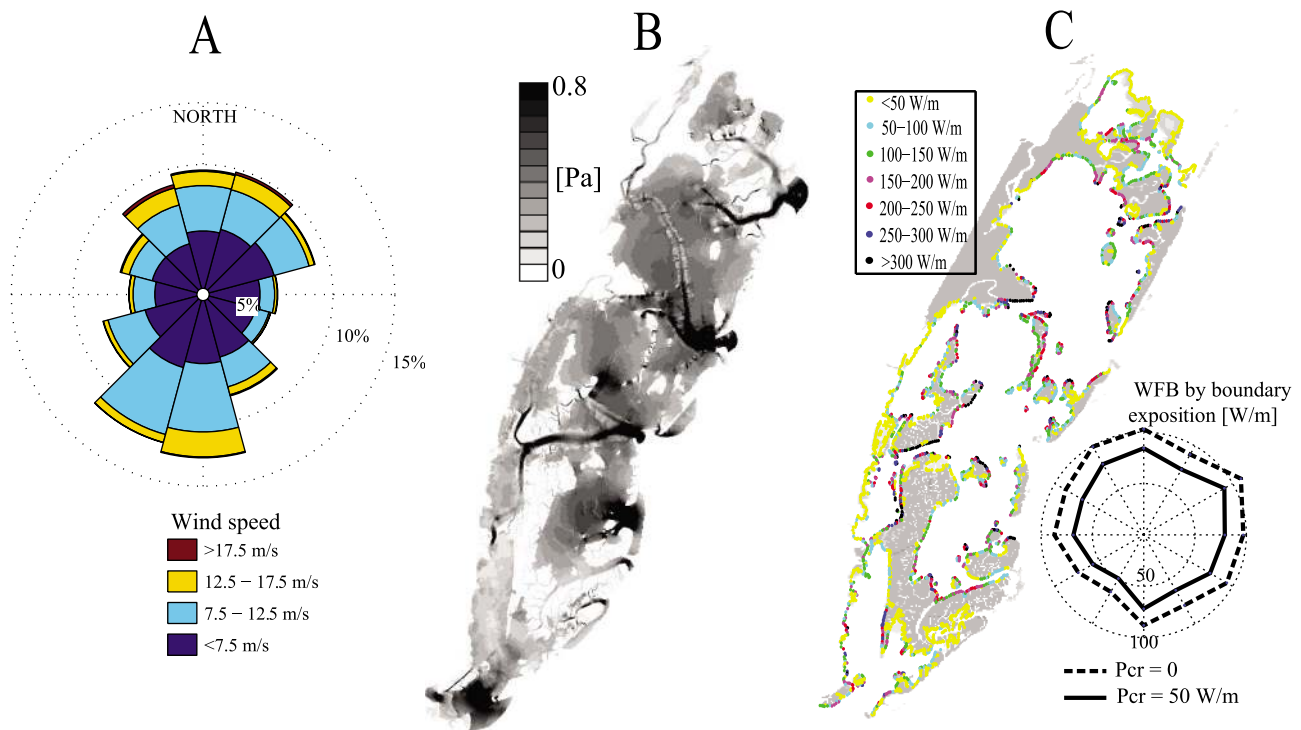
Figure 11. (a) Wind statistics, binned by four speeds and 12 directions; data are from NOAA Station CHLV2 during 1996 to 1999. (b) Total bottom shear stress on the tidal flats and (c) wave power at the marsh boundary with $P_{cr} = 0$ weighted with the wind distribution in Figure 11a. Wave Factor at the marsh Boundary (WFB) as a function of marsh boundary exposure weighted with the wind distribution in Figure 11a, for P_{cr} equal to 0 and 50 W/m.

wave erosion (P_{cr}) is set greater than zero. With a P_{cr} of 50 W/m the marsh boundary facing 0–90N receives 50% more wave power than the one facing 180 to 270 N.

8. Wave Action and Sea Level Rise

[47] Our results indicate that the wave regime inside the lagoon is sensitive to water depth and therefore oscillations in sea level. The effect of RSLR is assessed herein by running a set of simulations with increased water elevations at the seaward boundary. As sea level rises, both EF and WFB increase independent of wind direction (Figure 12). However, the variation is almost negligible for EF while it is significant for WFB. For simplicity, we focus only on wind blowing from 30°N, which is typical for strong winds and produces high values for EF and WFB (Figure 13). For every value of RSLR, WFB increases almost 10 times more than EF. For example, for a RSLR of 20 cm, WFB increases by 30%, while EF increases less than 5% with respect to normal conditions.

[48] We calculate the tidal prism by integrating the water discharge at the inlets over a tidal cycle. Tidal prism increases with RSLR (Figure 12c): for example a RSLR of 15 cm increase the tidal prism by 5%, independently of wind direction.

9. Discussion

[49] The model reproduces correctly water depth oscillations inside the lagoon. The best agreement between mea-

sured and calculated wave height is found at higher values of wind speed (Period 2, Figure 3). Some disagreement in wave height is found at low wind speeds (Period 1, Figure 2), which could be explained by a higher spatial variability in the wind field that is characteristic of low wind conditions and is not detectable with a single wind measurement point.

[50] The model assumes a steady wind forcing. For wind speed events with maximum winds speeds greater than 10 m/s and a maximum change in wind direction of ±30°, the average duration is 2.5 h (Table 2). This time interval is shorter than a tidal cycle (~12.4 h), therefore averaging over a tidal cycle is not exact. However there is no correlation between water level and wind speed ($r = 0.04$) which means that the same meteorological condition (i.e., wind speed) can occur at different moments during the tide oscillation when the basin is experiencing different water levels. Therefore we can assume that the average of the effect over the tidal cycle represents the ensemble average of different storm events forcing the lagoon at different moments.

[51] Although wave-induced bottom shear stresses are larger than those induced by tidal currents, the latter plays a significant role in the bottom shear stress distribution by increasing the peak values of the bottom shear stress by up to 40% (Figure 6). Therefore the use of a complete hydrodynamic model, which correctly reproduces tidal currents, is fundamental to study the morphological evolution of shallow water lagoons, and both components (waves and tidal currents) should always be taken into account.
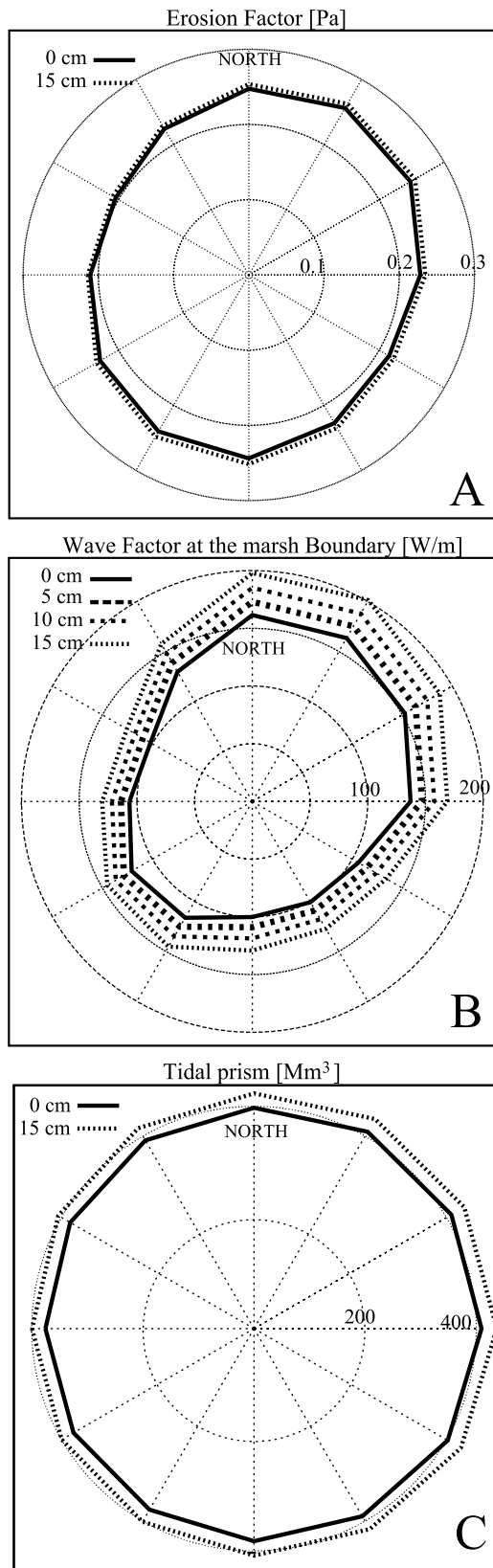
[52] The wave regime in shallow lagoons is controlled by wind conditions: wind speed determines the potential energy input to the waves, while wind direction determines the fetch, a proxy for the actual energy that can be transferred to the water body from the wind. Storm surge affects water level strongly in the lagoons (up to 0.6 m of super-elevation, Figure 4) and wind-wave propagation and decay depend on water level (4). As a consequence, storm surge is a key factor controlling the wave regime in the lagoons. Because storm surge depends on wind conditions, (Figure 4), the global wave regime is correlated strongly with wind speed and direction. The dependence of EF on wind direction is mainly due to variations in fetch: EF is greatest for winds blowing along the main basin axis, which offers the longest fetch (Figure 7b and Figure 8a). EF is also dependent on storm surge: positive (negative) storm surge results in higher (lower) EF. Storm surge has a dual effect on bottom shear stress. The effect of a positive (negative) storm surge is to increase (decrease) water depth, and to increase (decrease) wave height. Since higher (lower) wave heights augment bottom shear stresses, while higher (lower) water depths reduce them, the two processes compensate each other. The increase in EF associated with positive storm surge means that the wave effect is greater than the depth attenuation effect.

[53] The dependence of WFB on wind direction is due to its association with storm surge: WFB is greatest for winds that produce the highest positive storm surge (Figures 8b, 8d), while lower values are found for negative storm surges. This tendency is explained by the monotonic relationship among water level, wave height, and wave power at the marsh boundary: positive (negative) storm surges increase water depth, which increases (decreases) wave height leading to an increase (decrease) of wave power at the marsh boundary.

[54] Computed wave energy is not uniform along the marsh boundary, but is greater where the boundaries are oriented toward the northeast (Figure 11c). This result is in
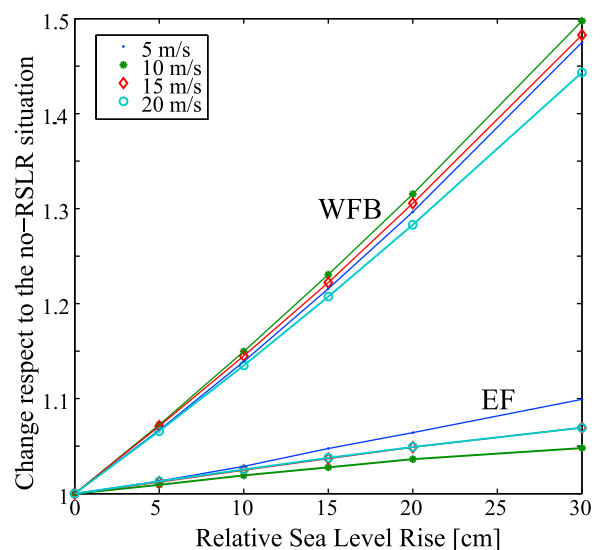

Figure 12. Erosion factor and wave factor at the marsh boundary calculated with a wind speed of 10 m/s and different values of RSLR.

Figure 13. WFB and EF computed of a function of RSLR and normalized by the value of WFB and EF with no RSLR. The values are computed for four different wind speeds for one direction, 30°N.

Table 2. Wind Duration Statistics[a]

Wind Speed Threshold Defining an Event	Wind Angle Defining an Event			
	30°	60°	90°	180°
5 m/s	2.9 h	4.3 h	5.1 h	14.1 h
10 m/s	2.5 h	2.9 h	3.1 h	5.7 h
15 m/s	1.8 h	1.9 h	1.9 h	3.1 h

[a]A wind event is defined as an uninterrupted sequence of wind conditions in which the wind speed does not go below the wind speed threshold and the direction does not change more than a specific angle respect to the initial direction.

accordance with the distribution of WFB, which is maximal for wind blowing from NE (Figure 8b). This means that even if statistically there are two dominant winds blowing from opposite directions (Figure 11a), the winds blowing from NE are predominant in determining the wave power at the marsh boundary. This distribution could induce an asymmetry in the marsh boundary erosion: assuming a constant erodibility over the whole marsh boundary, a higher erosion rate is expected on marsh boundaries that face the northeast. On the other hand, spatial variability in marsh erodibility, due to intrinsic differences in geotechnical properties as grain composition, compaction and vegetation, could induce a different trend in marsh boundary erosion. For example, marshes near barrier islands are likely to have a higher fraction of sand with respect to inner lagoon salt marshes. Further work will be done analyzing marsh characteristics and erosion rates at different sites.

[55] The asymmetry in WFB is caused mainly by the asymmetry in storm surge (which is correlated with wind speed and direction, Figure 4), rather than an asymmetry in basin geometry. Since storm surge is driven in part by regional upwelling/downwelling (e.g., Ekman transport), and not related specifically with this location, it is probable that other basins would experience the same asymmetry on WFB.

[56] EF is more uniform across the basin than is WFB, with slightly higher values of EF far from the marsh boundaries than closer to them.

[57] The effect of RSLR is to increase both EF and WFB (Figure 12), however the response of WFB is about 10 times greater than that of EF (Figure 13). The relationship among RSLR, water depth, wave height, WFB, and EF is analogous to the case of storm surge. WFB increases monotically with wave height, which is enhanced by the greater water depth induced by RSLR. EF is affected positively by the increase in wave height, but negatively by the increase in water depth.

[58] This dual behavior could affect the geomorphological evolution of the lagoon (Figure 14). RSLR will increase the erosion at the marsh boundaries, accelerating their retreat. The effect on the tidal flats, even if small, is to increase erosion and thus deepen them. Since tidal flat deepening increases water depth, a positive feedback is established. On the other hand, an increase in WFB would accelerate marsh boundary retreat, thereby augmenting sediment availability in the basin. The fate of the eroded sediment is difficult to forecast because of the extreme mobility of the suspended sediment. However, we expect that an increase in sediment availability would increase the deposition rate in the tidal

flats, creating a virtual decrease in RSLR and therefore a negative feedback.

[59] The fate of the lagoon depends on the relative strength of these two feedbacks. If the erosion rate in the tidal flats is greater than the increased deposition rate, then a global positive feedback will be established and marsh retreat will accelerate until they disappear, while tidal flats will keep on deepening. A stable condition will eventually occur only when tidal flats become deep enough to eliminate the effect of wave induced bottom shear stress [*Fagherazzi et al.*, 2006; *Marani et al.*, 2007; *Carniello et al.*, 2009b].

[60] On the other hand, if increased sediment availability increases deposition rates sufficiently to compensate for the increased bottom erosion, then a negative feedback will be established. This situation would lead to a temporary stable equilibrium, where the tidal flat depth is constant and RSLR is compensated by an increase in marsh boundary erosion rate. In this case, the morphologic evolution would again be characterized by marsh boundary retreat but at slower rate than for the previous scenario. The tidal flat equilibrium would last as long as the sediment supply by salt marsh retreatment balances tidal flat erosion.

[61] Boundary erosion would also change the fetch distribution and therefore the wave field. However, since the waves are controlled more by water-depth than by fetch, and since the increase in fetch is small, this effect is not expected to be significant.

[62] Positive RSLR increases the tidal prism (Figure 12c). This is explained by the characteristic flat topographic
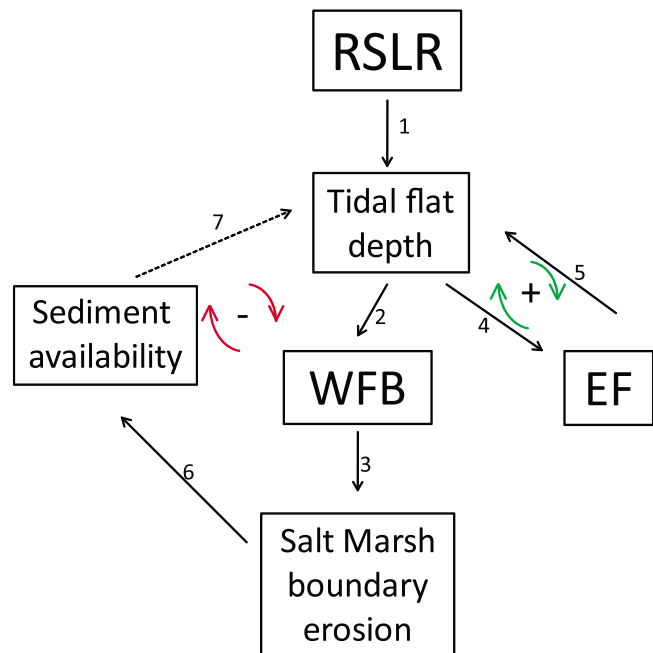

Figure 14. Effect of RSLR on basin morphology. RSLR increases water depth (1), which increases WFB (2), leading to marsh boundary erosion (3). Two feedbacks are present. Positive feedback: increasing water depth increases EF (4), which increases bottom erosion (5). Negative feedback: marsh erosion produces sediment (6), which deposit in the tidal flats and decrease water depth (7).

profile of salt marshes: when they become flooded, a significant volume of water is added to the tidal prism. The enlarging of tidal prism by RSLR is in accordance with other studies [*Mota Oliveira*, 1970; *O'Brien*, 1969]. In large estuaries, where hydrodynamics are controlled strongly by river discharge, an increase in water depth (by RSLR) results in lower currents [*Meade*, 1969], with a consequent reduction in sediment export and an increase in sedimentation, which compensate for the RSLR. In contrast, in shallow tidal bays lacking a significant source of freshwater and sediment, like the VCR lagoons, an increase in tidal prism will strengthen the tidal currents and enlarge the size of the tidal inlet [*Jarrett*, 1976; *D'Alpaos et al.*, 2010].

[63] In the VCR offshore sources of sediment are small [*Boon and Byrne*, 1981; *Nichols and Boon*, 1994] from river discharge and associated sediment loads [*Robinson*, 1994; *Nichols and Boon*, 1994; *Boynton et al.*, 1996]. Sediment contributions from marsh erosion are larger, but still relatively small [*Boon and Byrne*, 1981; *Nichols and Boon*, 1994]: most of the sediment erosion, deposition and transport within the lagoons is associated with sediment redistribution. EF shows a little difference between flood and ebb (around few percent, result not reported), so sediment resuspension inside the lagoon will not differ significantly from flood to ebb. Given these conditions, an increase in the volume of water exchanged with the sea will increase sediment export. In addition, the increase in the tidal prism will increase the ebb-tidal delta volume [*Walton and Adams*, 1976], and remove sand from the lagoons system [*FitzGerald et al.*, 2006]. Therefore RSLR, through tidal prism increase, will enhance sediment export, which will add to the increase erosion of the tidal flat and marsh boundary.

10. Conclusions

[64] We applied the numerical hydrodynamic model WWTM to the lagoons of the Virginia Coast Reserve and we tested it with measured water levels and wave heights and periods. We used the model to forecast wave action within the lagoons for varying wind conditions and RSLR and drew the following conclusions:

[65] 1. For each wind speed, the total bottom shear stress over the tidal flats is driven by fetch, while the wave power at the marsh boundary is controlled by water depth. Storm surge, by increasing water level inside the lagoons, plays a fundamental role in the marsh boundary erosion.

[66] 2. The expected wave power at the marsh boundary is greatest at the boundaries exposed toward the NE. Nonuniform marsh boundary erosion is therefore predicted in the lagoon system.

[67] 3. The effect of RSLR is to increase both tidal flat erosion (EF) and salt marsh boundary erosion (WFB). However, the relative increase in the latter is almost ten times greater than the former.

[68] 4. A positive feedback is expected between RSLR and lagoon bottom erosion because of the increase of EF, while a negative feedback is expected between RSLR and lagoon bottom erosion as a consequence of the sediment provided by marsh boundary deterioration. If the global feedback is positive, then salt marsh edges are eroded and tidal flats deepen in the basin. If the global feedback is negative, then the tidal flats find a temporary equilibrium state with RSLR thanks to the sediment supply from the marsh boundary erosion.

References

Allen, J., P. Somerfield, and F. Gilbert (2007), Quantifying uncertainty in high-resolution coupled hydrodynamic-ecosystem models, *J. Mar. Syst.*, *64*(1–4), 3–14.

Boon, J. D. (2004), *Secrets of the Tide: Tide and Tidal Current Analysis and Applications*, Storm Surges and Sea Level Trends, 210 pp., Horwood, Chichester, U. K.

Boon, J. D., and R. J. Byrne (1981), On basin hypsometry and the morphodynamic response of coastal inlet systems, *Mar. Geol.*, *40*, 27–48.

Boynton, W. R., J. D. Hagy, L. Murray, C. Stokes, and W. M. Kemp (1996), A comparative analysis of eutrophication patterns in a temperate coastal lagoon, *Estuaries*, *19*, 408–421.

Breugem, W. A., and L. H. Holthuijsen (2007), Generalized shallow water wave growth from Lake George, *J. Waterw. Port Coastal Ocean Eng.*, *133*(3), 173–182.

Cappucci, S., C. L. Amos, T. Hosoe, and G. Umgiesser (2004), SLIM: A numerical model to evaluate the factors controlling the evolution of intertidal mudflats in Venice lagoon, Italy, *J. Mar. Syst.*, *51*, 257–280.

Carniello, L., A. Defina, S. Fagherazzi, and L. D'Alpaos (2005), A combined wind wave-tidal model for the Venice lagoon, Italy, *J. Geophys. Res.*, *110*, F04007, doi:10.1029/2004JF000232.

Carniello, L., A. D'Alpaos, and A. Defina (2009a), Simulation of wind waves in shallow microtidal basins: Application to the Venice lagoon, Italy, in *Proceedings of 6th IAHR Symposium on River, Coastal and Estuarine Morphodynamics: RCEM 2009*, edited by C. A. Vionnet et al., pp. 907–912, Taylor Francis, London.

Carniello, L., A. Defina, and L. D'Alpaos (2009b), Morphological evolution of the Venice Lagoon: Evidence from the past and trend for the future, *J. Geophys. Res.*, *114*, F04002, doi:10.1029/2008JF001157.

Christie, M. C., and K. R. Dyer (1998), Measurements of the turbid edge over the Skeffling mudflats, in *Sedimentary Processes in the Intertidal Zone, Geol. Soc. Spec. Publ.*, vol. 139, edited by K. S. Black, D. M. Paterson, and A. Cramp, pp. 45–55, Geol. Soc. of London, London.

D'Alpaos, A., S. Lanzoni, M. Marani, and A. Rinaldo (2010), On the tidal prism–channel area relations, *J. Geophys. Res.*, *115*, F01003, doi:10.1029/2008JF001243.

D'Alpaos, L., and A. Defina (2007), Mathematical modeling of tidal hydrodynamics in shallow lagoons: A review of open issues and applications to the Venice lagoon, *Comput. Geosci.*, *33*, 476–496, doi:10.1016/j.cageo.2006.07.009.

Defina, A. (2000), Two-dimensional shallow water equations for partially dry areas, *Water Resour. Res.*, *36*, 3251–3264.

Defina, A., L. Carniello, S. Fagherazzi, and L. D'Alpaos (2007), Self organization of shallow basins in tidal flats and salt marshes, *J. Geophys. Res.*, *112*, F03001, doi:10.1029/2006JF000550.

Emory, K. O., and D. G. Aubrey (1991), *Sea Levels, Land Levels and Tide Gauges*, Springer, New York.

Fagherazzi, S., and P. L. Wiberg (2009), Importance of wind conditions, fetch, and water levels on wave generated shear stresses in a shallow intertidal basin, *J. Geophys. Res.*, *114*, F03022, doi:10.1029/2008JF001139.

Fagherazzi, S., L. Carniello, L. D'Alpaos, and A. Defina (2006), Critical bifurcation of shallow microtidal landforms in tidal flats and salt marshes, *Proc. Natl. Acad. Sci. U. S. A.*, *103*(22), 8337–8341.

Fagherazzi, S., C. Palermo, M. C. Rulli, L. Carniello, and A. Defina (2007), Wind waves in shallow microtidal basins and the dynamic equilibrium of tidal flats, *J. Geophys. Res.*, *112*, F02024, doi:10.1029/2006JF000572.

FitzGerald, D. M., I. V. Buynevich, and B. A. Argow (2006), Model of tidal inlet and barrier island dynamics in a regime of accelerated sea-level rise, *J. Coastal Res.*, *39*, 789–795.

Fredsoe, J., and R. Deigaard (1993), *Mechanics of Coastal Sediment Transport*, Adv. Ser. Ocean Eng., vol. 3, 392 pp., World Sci., Singapore.

Hayden, B. P., C. F. V. M. Santos, G. Shao, and R. C. Kochel (1995), Geomorphological controls on coastal vegetation at the Virginia Coast Reserve, *Geomorphology*, *13*(1–4), 283–300, doi:10.1016/0169-555X(95)00032-Z.

Holthuijsen, L. H., N. Booij, and T. H. C. Herbers (1989), A prediction model for stationary, short-crested waves in shallow water with ambient currents, *Coastal Eng.*, *13*, 23–54.

Jarrett, J. T. (1976), Tidal prism—Inlet area relationships, *Gen. Invest. Tidal Inlets Rep. 3*, 32 pp., U.S. Army of Corps of Eng., Washington, D. C.

Kamphuis, J. W. (1975), Friction factor under oscillatory waves, *J. Waterw. Harbors Coastal Eng. Div. Am. Soc. Civ. Eng.*, *101*, 135–144.

Lawson, S. E. (2004), Sediment suspension as a control on light availability in a coastal lagoon, M.S. thesis, 119 pp., Univ. of Va., Charlottesville, Va.

Lawson, S. E. (2008), Physical and biological controls on sediment and nutrient fluxes in a temperate lagoon, Ph.D. dissertation, 187 pp., Univ. of Va., Charlottesville, Va.

Lawson, S. E., P. L. Wiberg, K. J. McGlathery, and D. C. Fugate (2007), Wind-driven sediment suspension controls light availability in a shallow coastal lagoon, *Estuaries Coasts*, *30*(1), 102–112.

Le Hir, P., W. Roberts, O. Cazaillet, M. Christie, P. Bassoullet, and C. Bacher (2000), Characterization of intertidal flat hydrodynamics, *Cont. Shelf Res.*, *20*(12–13), 1433–1459.

Marani, M., A. D'Alpaos, S. Lanzoni, L. Carniello, and A. Rinaldo (2007), Biologically-controlled multiple equilibria of tidal landforms and the fate of the Venice lagoon, *Geophys. Res. Lett.*, *34*, L11402, doi:10.1029/2007GL030178.

Mariotti, G., and S. Fagherazzi (2010), A numerical model for the coupled long-term evolution of salt marshes and tidal flats, *J. Geophys. Res.*, *115*, F01004, doi:10.1029/2009JF001326.

Meade, R. H. (1969), Landward transport of bottom sediment in estuaries of the Atlantic coastal plain, *J. Sediment Petrol.*, *39*, 222–234.

Moeller, I., T. Spencer, and J. R. French (1996), Wave attenuation over saltmarsh surfaces: Preliminary results from Norfolk, England, *J. Coastal Res.*, *12*(4), 1009–1016.

Möller, I., T. Spencer, J. R. French, D. J. Leggett, and M. Dixon (1999), Wave transformation over salt marshes: A field and numerical modelling study from north Norfolk, England, *Estuarine Coastal Shelf Sci.*, *49*(3), 411–426.

Mota Oliveira, I. B. (1970), Natural flushing ability in tidal inlets, paper presented at 12th Coastal Engineering Conference, Am. Soc. of Civ. Eng., Washington, D. C.

Nerem, R., T. van Dam, and M. Schenewerk (1998), Chesapeake Bay subsidence monitored as wetland loss continues, *Eos Trans. AGU*, *79*, 149.

Nichols, M. M., and J. D. Boon (1994), Sediment transport processes in coastal lagoons, in *Coastal Lagoon Processes*, edited by B. Kjerfve, pp. 157–217, Elsevier, New York.

O'Brien, M. P. (1969), Equilibrium flow areas of inlets on sandy coasts, *J. Waterw. Harbors Coastal Eng. Div. Am. Soc. Civ. Eng.*, *95*, 43–55.

Oertel, G. F. (2001), Hypsographic, hydro-hypsographic and hydrological analysis of coastal bay environments, Great Machipongo Bay, Virginia, *J. Coastal Res.*, *17*(4), 775–783.

Oertel, G. F., G. T. F. Wong, and J. D. Conway (1989), Sediment accumulation at a fringe marsh during transgression, Oyster, Virginia, *Estuaries*, *12*, 18–26.

Press, W. H., S. A. Teukolsky, W. T. Vetterling, and B. P. Flannery (1992), *Numerical Recipes*, 2nd ed., Cambridge Univ. Press, Cambridge, U. K.

Robinson, S. E. (1994), Clay mineralogy and sediment texture of environments in a barrier island-lagoon system, M.S. thesis, 102 pp., Univ. of Va., Charlottesville, Va.

Schwimmer, R. A. (2001), Rates and processes of marsh shoreline erosion in Rehoboth Bay, Delaware, U.S.A., *J. Coastal Res.*, *17*(3), 672–683.

Schwimmer, R. A., and J. E. Pizzuto (2000), A model for the evolution of marsh shorelines, *J. Sediment. Res.*, *70*(5), 1026–1035.

Soulsby, R. L. (1995), Bed shear-stresses due to combined waves and currents, in *Advances in Coastal Morphodynamics*, edited by M. J. F. Stive et al., pp. 4-20–4-23, Delft Hydraul., Delft, Netherlands.

Soulsby, R. L. (1997), *Dynamics of Marine Sands: A Manual for Practical Applications*, 248 pp., Thomas Telford, London.

Tilburg, C. E., and R. W. Garvine (2004), A simple model for coastal sea level prediction, *Weather Forecasting*, *19*(3), 511–519.

Umgiesser, G., D. M. Canu, A. Cucco, and C. Solidoro (2004), A finite element model for the Venice Lagoon: Development, set up, calibration and validation, *J. Mar. Syst.*, *51*(1–4), 123–145, doi:10.1016/j.jmarsys.2004.05.009.

U.S. Army Coastal Engineering Research Center (1984), *Shore Protection Manual*, Washington, D. C.

Walton, T. L., and W. D. Adams (1976), Capacity of inlet outer bars to store sand, paper presented at Fifteenth Coastal Engineering Conference, Am. Soc. of Civ. Eng., Honolulu, 11–17 Jul.

Whitehouse, R. J. S., and H. J. Mitchener (1998), Observations of the morphodynamic behaviour of an intertidal mudflat at different timescales, in *Sedimentary Processes in the Intertidal Zone*, *Geol. Soc. Spec. Publ.*, vol. 139, edited by K. S. Black, D. M. Paterson, and A. Cramp, pp. 45–55, Geol. Soc. of London, London.

Young, I. R., and L. A. Verhagen (1996), The growth of fetch-limited waves in water of finite depth. Part 1: Total energy and peak frequency, *Coastal Eng.*, *29*(1–2), 47–78.

L. Carniello and A. Defina, Department IMAGE, University of Padova, Via Loredan 20, I-35131 Padova, Italy.

S. Fagherazzi and G. Mariotti, Department of Earth Sciences, Boston University, 675 Commonwealth Ave., Boston, MA 02215, USA. (giuliom@bu.edu)

K. J. McGlathery and P. L. Wiberg, Department of Environmental Sciences, University of Virginia, Clark Hall, 291 McCormick Rd., PO Box 400123, Charlottesville, VA 22904-4123, USA.